RSC Advances

ROYAL SOCIETY OF CHEMISTRY

www.rsc.org/advances

A novel interfacial synthesis of MnO-NiO-reduced graphene oxide hybrid with enhanced pseudocapacitance performance

Weidong Liu[1], *Xiaobing Wang*[1], *Lishu Zhang, and Jianshe Lian**

Key Laboratory of Automobile Materials (Jilin University), Ministry of Education and School of Materials Science and Engineering, Jilin University, Changchun 130022, China.

Corresponding author: Jianshe Lian

E-mail: lianjs@jlu.edu.cn

Tel: (+86)431-85095875

Fax: (+86)431-85095876

Abstract

We demonstrate a facile one-step interface approach to in-situ grow MnO-NiO nanoparticles on reduced graphene oxide via a DMF-water double solvent system without any addition agent. The dispersed MnO-NiO nanoparticles provide high theoretical capacitance. The uniform growth and attachment of MnO-NiO nanoparticles on the graphene nanosheets offer greatly decreased contact resistance and effective charge transfer. Simultaneously, graphene plays an architecture support role to ensure stable structure. Electrochemical measurement results show that the MNG electrodes deliver a high specific capacitance of 813F g^{-1} at 0.5 A g^{-1}, excellent rate capability (80.56% retention at 4 A g^{-1}) and good cycling stability. In the one-step interface approach, the excellent dissolving capacity of DMF allows inorganic salts directly used as reagents in organic phase instead of conventional organic reagents, which fundamentally reduces the internal resistances of the electrode active materials. By virtue of this significant expansion of reagent categories and the convenient experimental accessibility, this improved interface method might be a promising approach to develop other classes of hybrids based on graphene for electrochemical energy storage devices and readily to scale up.

KEYWORDS: improved interface method, MnO-NiO nanoparticles, graphene, supercapacitors

Introduction

In recent decades, researchers have paid great endeavor to study alternative energy storage/conversion devices with high power and energy densities, in order to relieve the issues about the mounting environmental concerns and the stressed-out fossil fuels.[1-3] Compared with other power devices, supercapacitors, having attracted a lot of attention due to their higher power densities,[4] have sufficient research foundation and the potential to impel the current energy storage technology.[5]

Generally accepted, the electrochemical activity and kinetic feature of electrode materials play a vital role in acquiring the high performance of supercapacitors.[6] Transition metal oxides, acting as important electrode materials, have attracted extensive attention owing to their high specific capacitances. Whereas most of active transition metal oxide electrode materials (e.g. MnO_2,[7-9] TiO_2,[10] NiO,[11] and Co_3O_4[12]) have inherently low conductivity and/or dissatisfactory structures that result in poor ability of electron transfer and unsatisfactory electrochemical performance.[13] In this respect, the combination of Mn/Ni oxides can be expected for superior activity. The synergistic effect between the two metal oxides can decrease the internal resistance of their composites. Furthermore, manganese oxides and nickel oxides, as the electrode materials, could be optimized by structure and surface modification to acquire perfect physicochemical properties for large-scale applications.[14] The advantages of porosity

and high surface area of nickel oxides could availably make up the morphology shortage of manganese oxide so that electrolyte can smoothly permeate into the electrode material.[15-17] In addition, manganese and nickel oxides have following advantages, for instance, high specific capacitance, low material cost, abundance and environmentally benign nature. Nonetheless, manganese and nickel oxides as supercapacitor electrode materials are still limited by the ordinary conductivity and structure stability. To solve these issues, graphene has been used as a carbon support for metal oxide for the electrode material of supercapacitors due to its excellent conductivity, suitable lamellar morphology and the ability of supplying charge storage.[18, 19]

Based on the considerations above, we developed a novel and facile one-step interface method to fabricate the MnO-NiO-rGO hybrid (rGO = reduced graphene oxide) as the electrode material for supercapacitors. Compared to conventional interface methods, N,N-dimethylformamide (DMF) has been introduced to replace the previous water-insoluble organic phase solvent, like CCl_4[20] and CH_2Cl_2,[21] as the solvent for metal inorganic salts, which could bring the following advantages: (1) It can effectively solve the large-scale agglomeration by reducing local reaction area and further total reaction rate;[20] (2) Some common drawbacks in conventional interface method such as the addition of structure directing agents,[22] and the

complicated experimental process[23] were avoided; (3) Owing to the low dissolution rate between DMF and aqueous solutions, a banded micellar zone formed between two phases instead of the conventional bidimensional phase interface, which promoted the synthetic efficiency; (4) The metal inorganic salts dissolved in DMF replaced the conventional organic reagents and further reduced the internal resistance of the active material. The electrochemical properties of all as-obtained samples were investigated. The as-prepared MnO-NiO-rGO electrode samples have shown dramatically enhanced electrochemical performance such as high specific capacitance, excellent rate capability and conductivity, and good cycling stability.

2. Experimental Section

2.1 Chemicals and materials

All solvents and chemicals were analytical pure and used without further purification. The solvents and chemicals were purchased from Sinopharm Chemical Reagent Co., Ltd.

2.2 Synthesis of MNG hybrid by the improved interface method

Modified Hummers method was utilized to fabricate graphite oxide (GO) with powdered flake graphite (325 mesh).[24, 25]

The called improved interface method was used to one-step synthesize MNG hybrid, which is described as follows. Deionized water was utilized in all the experimental procedures. First, GO (150 mg) was dispersed in 50 mL DMF solvent

and sonicated for 120 min. Based on the molar ratio of Mn and Ni (3:2), $Mn(CH_3COO)_2$ (0.09 M) and $Ni(NO_3)_2$ (0.06 M) were dissolved into the solution above with mechanical stirring for 30 min to mix uniformly. Next, the mixed solution was slowly added into an equal volume of Na_2O_2 aqueous solution (0.4 M) prepared in advance. Subsequently, the whole reaction system experienced a standing and ageing process for 12 h at room temperature. The precipitates were collected by centrifugation at 8000 rpm and repetitively rinsed with deionized water and ethyl alcohol, respectively. Afterwards, the obtained precipitates were added into a 100 ml sodium borohydride ($NaBH_4$) aqueous solution with mechanical stirring for 1 h at a 353 K water-bath temperature to restore GO to graphene. After a similar centrifugal cleaning process with deionized water and ethyl alcohol, the precipitates were dried in a vacuum oven at 333 K for 12 h and then sufficiently grinded to obtain powder samples. Finally, the products were annealed at 623 K for 10 min at a heating rate of 1K min^{-1} in a tubular vacuum furnace with nitrogen atmosphere and then furnace cooled down to room temperature. Thus the final MnO-NiO-rGO hybrid was produced and termed MNG. Furthermore, for comparison, we also synthesized the other three kinds of products by different methods or under different conditions. The MnO-NiO composites were prepared under the same conditions with MNG in the absence of graphene and termed MNO. The products of MnO-NiO composite were also fabricated by common coprecipitation method with or without magnetic stirring, and termed S and NS, respectively. All the samples were handled by annealing treatment at 623K and the details about the common coprecipitation products were demonstrated in Fig. S1 and S2, Supporting Information.

2.3 Material Characterizations

Powder X-ray diffraction (XRD) analyses were performed on a Rigaku D/max

2500pc X-ray diffractometer with Cu Kα radiation (λ=1.54156Å) at a scan rate of 4 ° min^{-1}. X-ray photoelectron spectroscopy (XPS) spectra were run on an ESCALAB Mk II (Vacuum Generators) spectrometer with unmonochromatized Al Kα X-rays (240W). Cycles of XPS measurements were conducted in a high-vacuum chamber with a base pressure of 1.33×10^{-6} Pa. Binding energies were standardized by assigning the value of the C 1s peak to 284.6 eV. Morphologies of the as-prepared samples were performed on a field emission scanning electron microscope (FESEM, JEOL JSM-6700F) and transmission electron microscopy (TEM), high-resolution TEM (HRTEM) and selected area electron diffraction (SAED) were characterized with a JEOL 2100F instrument. The Brunauer-Emmett-Teller (BET) specific surface areas and Barret-Joyner-Halenda (BJH) pore volumes of the samples were determined by N2 adsorption/desorption isotherms on a Micromeritics ASAP 2020 M apparatus with all samples degassed at 373 K for 12 h in vacuum before the measurement. Thermogravimetric analysis (TGA) was run on a TGA/SDT Q600 thermogravimetric analyzer from room temperature to 773 K at a heating rate of 10 K min^{-1} in air flow.

2.4 Electrochemical Measurements

The electrochemical characteristic of as-obtained products was measured with a conventional three-electrode electrolytic cell at room temperature. Platinum foil and a saturated calomel electrode (SCE) were used as the counter and reference electrodes,

respectively. The as-obtained MNG powders were mixed with acetylene black and polyvinylidene fluoride (PVDF, 5 wt %) binder with a mass ratio of 80:15:5. The mixture was dissolved in N-methylpyrrolidone (NMP) with stirring for 6 hours to make electrode slurry which was coated onto nickel foam current-collectors (A=1.0 cm^2) to manufacture the working electrode samples. These samples were dried in vacuum atmosphere at 383 K for 12 h for further use. The weight of the active material on each sample was about 3~4 mg. Before the electrochemical measurement, the electrode samples were soaked in a solution mixture of deionized water and ethyl alcohol (volume ratio 1:1) and a 3 M KOH aqueous solution, successively, for both 12 h. The cyclic voltammogram (CV), electrochemical impedance spectroscopy (EIS) and galvanostatic charge discharge (GCD) measurements were completed with a CHI 660B electrochemical workstation (Shanghai CH Instrument Company, China) with 3 M KOH aqueous solution as the electrolyte.

3. Results and discussion

3.1 The formation mechanism of the MNG hybrid

The MNG hybrid was prepared by a novel one-step interface method by the introduction of DMF. DMF possesses superior dissolving capacity for inorganic reagents, including most of manganese salts and nickel salts, which own lower internal resistance than conventional organic reagents. Thus, the utilization of DMF

undoubtedly broke the restriction of reactant categories and improved the conventional interface method for substantially expanding the applied range and feasibility. This would be much beneficial to the capacitive properties of the as-obtained electrode material, especially at high rate charge/discharge processes.[26] The natural advantage of interface method was well remained in view of the effective solution of the agglomeration problem.

The reaction mechanism illustration of the improved interface method is sketched out in Fig. 1 (the left three cylindrical schematic diagrams). Fig. 1a~e show the phenomena of productive process of the MNG hybrid during different reaction time. It can be seen that at the initial phase of reaction (Fig. 1a), a narrow banded reaction interface formed rapidly, although its volume is still very small because of the short reaction time. Then after aging for 2h, the reaction interface gradually became blurred and expanded, just as the situation shown in the Fig. 1b and f; Afterwards, as time continued (Fig. 1c, d and e), the banded interface reaction zone became more and more obvious with its volume increasing. In addition, the products continuously precipitated into the lower aqueous phase probably due to the excessive accumulation of weight and the escape of bubbles generated from Na_2O_2 during the reaction process. As far as we speculate, the improved interface system is a combination of conventional interface system and a called micellar system. The formation of banded micellar zone can create plenty of microscopic reaction areas. These areas will slow the reaction rate as well as the diffusion rate of the reagents, resulting in nanoscale hybrid. The nanostructured architecture should supply more advantageous surface

area and accessibility between active materials and electrolyte compared to their other larger counterparts.[27, 28]

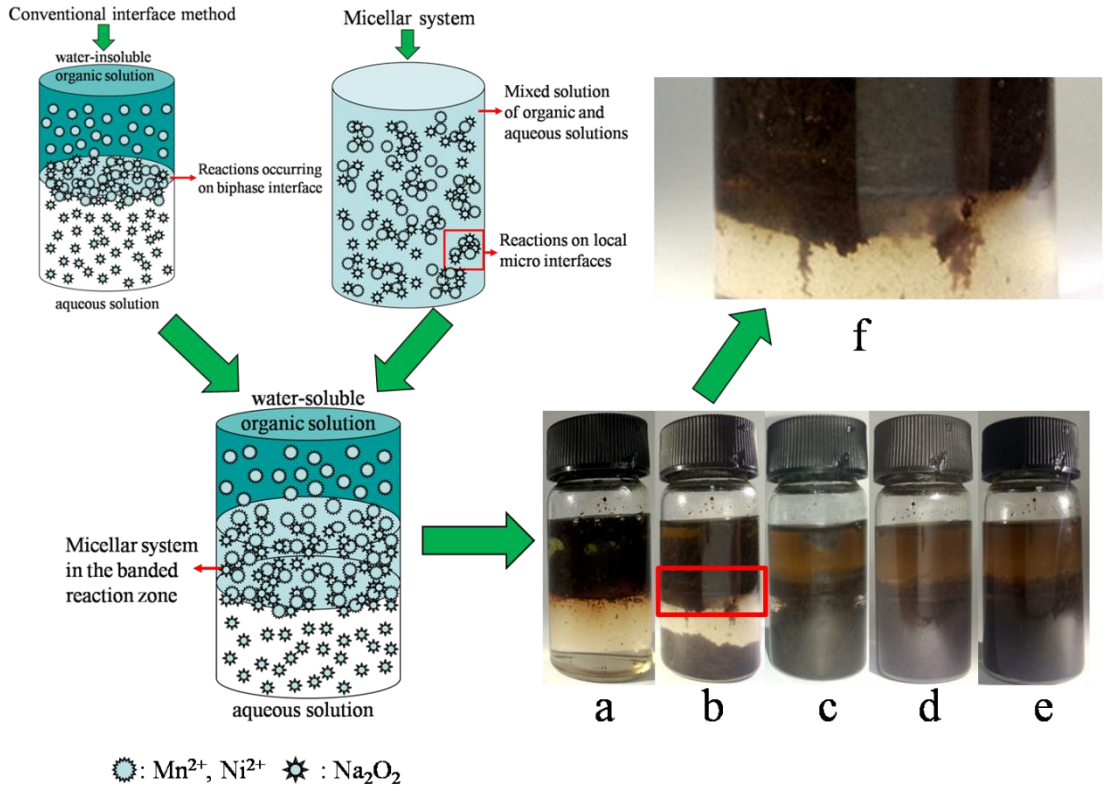

Fig. 1. The reaction mechanism diagram of the improved interface method and the phenomenon images of the reaction process of MNG hybrid ~~at~~ during different reaction time: (a) 0.1h, (b)2h, (c)4h, (d)6h, (e)8h and (f) the red rectangle area in b: the detail view of the banded interface reaction zone.

3.2 Characterization of MNO and MNG hybrids

The XRD patterns of graphite oxide (GO) and graphene (rGO) are shown in Fig. 2a. GO had a prominent characteristic peak at 2θ=10.58 °due to the presence of hydroxyl, epoxy, and carboxyl groups. After the reduction process, the characteristic peak changed to 2θ=25.04 °because of the removal of those oxygen-containing functional groups, indicating that GO was well restored to graphene.[29] The typical diffraction peaks in the XRD pattern of the MNG hybrid are shown in Fig. 2b, with each one

well locating in between the corresponding peak positions of NiO (JCPDS 73-1523) and MnO (JCPDS 75-0257).[30] So, the substance should be a compound of manganese and nickel oxide, most likely $Mn_{0.6}Ni_{0.4}O$ if the initial feeding ratio of Mn and Ni is taken into account (However, it is called MnO-NiO in the following). Notably, broad diffraction peaks with low intensities are shown in the (111), (200), (220) and (311) planes indicating the feature of low crystallinity. For electrode materials, low crystallinity means high density of grain boundaries with fine grains, which would provide more effective transmission channels for electrolyte ions.[26] Therefore, electrode materials with low crystallinity are able to increase material utilization and exhibit larger C_s than their high crystallinity counterparts.[21, 26, 31] The characteristic peak of graphene can't be seen in the MNG' XRD pattern probably owing to its low content and disordered structure in the MNG hybrid. So, the existence of graphene will be proven by the TGA, DSC and FT-IR measurements.

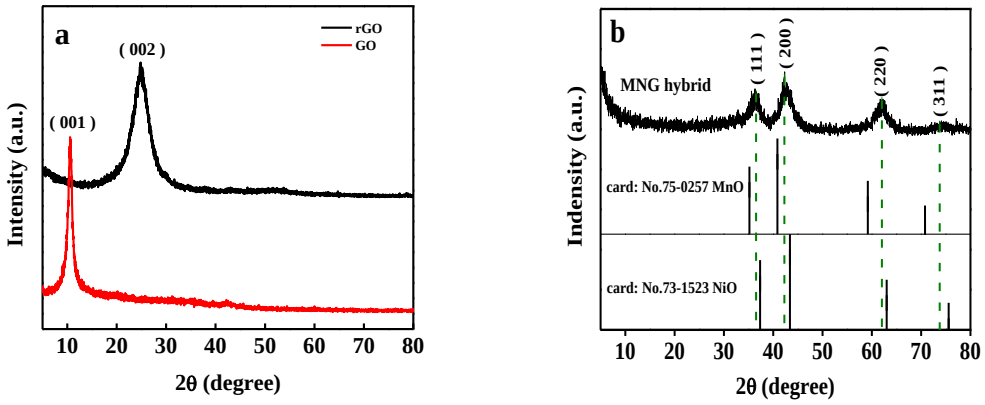

Fig. 2. XRD patterns of power samples: (a) graphene and GO; (b) MNG hybrid.

TGA and DSC measurements were carried out from 273 to 773K at a heating rate of 10K min^{-1} in air flow (Fig. 3) to depict the weight ratio of MnO-NiO and graphene in the MNG hybrid. The weight loss below 373K should owe to the elimination of

physically adsorbed water in the samples, which corresponds to the endothermic peak at around 371K on the DSC curve. Then the loss around 450K should be attributed to the wastage of labile oxygen containing functional groups, which leads to the formation of exothermic peak on the DSC curve.[21, 32, 33] As heating continues, the loss of graphene occurs in the temperature range from 523 to 773K. Universally, graphene are completely burned into CO_2 in air between 523K and 773K.[34] Graphene totally vanished while Mn-Ni hybrid remains unchanged after 773K; hence, the mass percentages of MnO-NiO hybrid and graphene were estimated to 85.97% and 14.03% (Fig. 3), respectively.

FT-IR spectra of the GO and the MNG are presented in Fig. 3b. The peaks at 3439 and 1119 cm^{-1} in the FT-IR spectrum of GO are attributed to O−H stretching vibration.[35, 36] The carbonyl/carboxyl C=O, aromatic C=C, epoxy C–O, alkoxy C–O and carboxyl C–O can be observed at 1726, 1631, 1385, 1163 and 1050 cm^{-1}, respectively.[37-39] These main characteristic peaks indicate that GO had been synthesized successfully. Compared with the FT-IR spectrum of GO, the peaks corresponding to various oxygen containing functional groups of rGO in the MNG hybrid disappeared or obviously decreased in intensity. Furthermore, some bands are associated with metal-oxygen stretching at low frequencies from 500 to 800 cm^{-1}.[40-42] The new broad peak at around 500 to 650 cm^{-1} corresponds to the vibration of the

Mn–O[22, 43] and the Ni-O[44, 45] stretching modes, of which the Mn-O associated with Mn in tetrahedral and octahedral sites. These results indicate that the as-synthesized MNG hybrid consists of disorderedly stacked graphene and MnO-NiO nanocomposites.

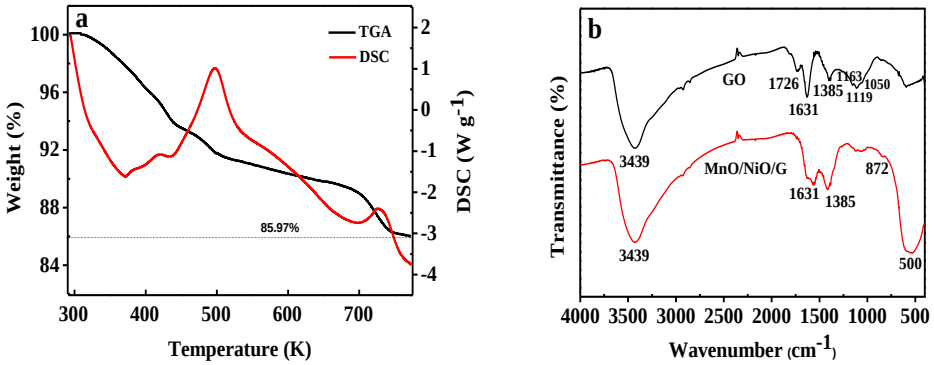

Fig. 3. (a) TGA/DSC curve of MNG; (b) FT-IR spectra of GO and MNG hybrid.

The composition of the as-obtained MNG hybrid and the valence states of Ni and Mn were investigated via X-ray photoelectron spectroscopy (XPS) measurement. In the survey scope, manganese, nickel, carbon, and oxygen were detected, shown in Fig. 4a. The C 1s peak of XPS spectrum (Fig. 4b) is divided into four functional groups: the C–C bond at 284.51 eV, the C–O bond at 285.65 eV, the carbonyl carbon in the C=O bond at 286.59 eV, and the carboxylate carbon in the O–C=O bond at 288.35 eV. An obvious reduction of the peak intensities at 285.59 and 288.35 eV is found, which reveals the effective elimination of most oxygenous hydroxyl and epoxide functional groups, corresponding well to the FTIR results.[39, 46] The binding energies for Mn $2p_{3/2}$

and Mn $2p_{1/2}$ are found to be 641.5 and 653.4 eV (Fig. 4c), respectively, which are in accordance with the spectrum of MnO. As for Ni (Fig. 3d), the $2p_{3/2}$ (855.21 eV) and $2p_{1/2}$ (873.22 eV) peaks together with two satellite peaks (861.17 and 879.57 eV) prove the presence of Ni^{2+} state corresponding to the formula of NiO. The analysis results of the above XPS spectrum is in good agreement with the XRD patterns on the components of the as-obtained hybrid. MnO and NiO coexist in the final nanoscale MNG hybrid products.

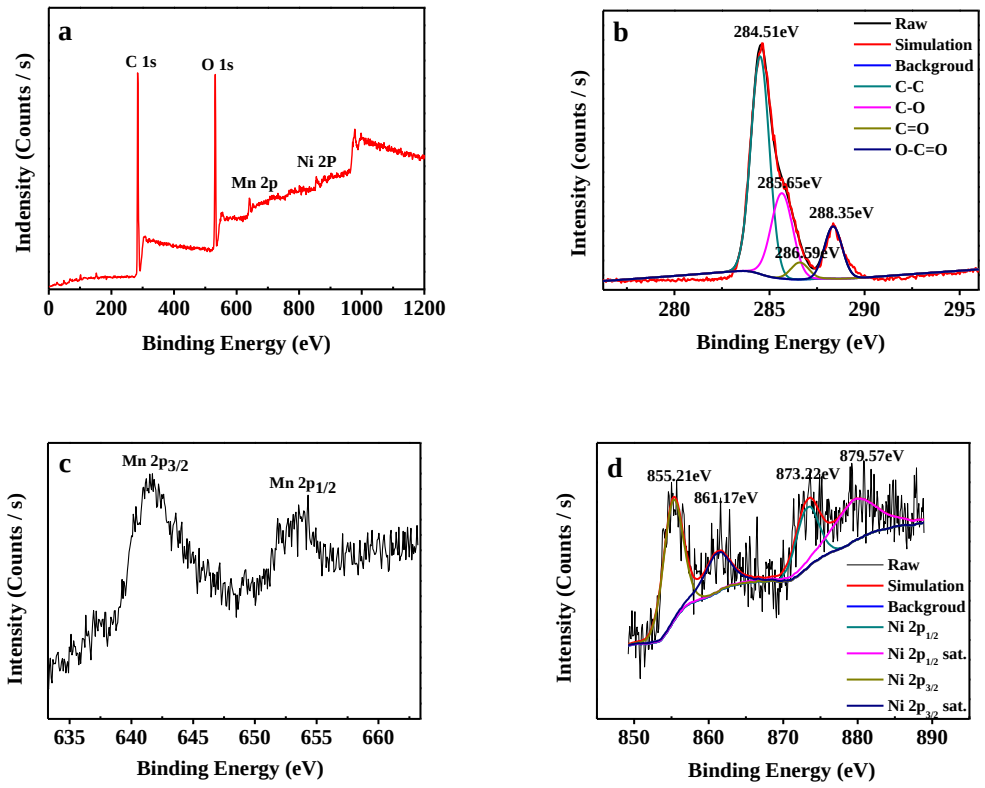

Fig. 4. XPS spectra of MNG powder samples: (a) survey scan; (b) C 1s region; (c) Mn 2p region and (d) Ni 2p region.

Further insight into the morphology of the MNG and MNO hybrids is visible from the field emission scanning electron microscopy (FESEM), transmission electron

microscopy (TEM) and HRTEM images (Fig. 5 and Fig. S3, Supporting Information). Both the MNG and MNO hybrids show nanoscale particles with homodisperse structure, but in different morphology. Such nanostructure forms large surface areas which should be beneficial to the fast transfer of electrons and ions and contribute much to the specific capacitance if using as electrode materials. As shown in Fig. 5a, many nanoparticles uniformly attach on the surface of graphene nanosheets rather than adhere together like the previous netlike nanostructure of the MNO (Fig. S3b, Supporting Information). Here, graphene plays a role of support frame. The functional groups located on the surfaces or edges of graphene nanosheets, like epoxy, hydroxyl, carbonyl and carboxyl, acting as anchor sites, facilitate the in-situ growth of MnO-NiO nanoparticles.[3] Thus, the nanoparticles are purposefully separated with each other and the agglomeration problem is successfully prevented. Fig. 5b shows the detailed FESEM image of the MNG hybrid with high density nanocomposites. The TEM image of the marginal area of MNG nanosheet is displayed in Fig. 5c. The graphene nanosheets and MnO-NiO nanoparticles are clearly observed. In the HRTEM image of Fig. 5d, two domains of size about 10nm or less with different crystal orientation between them can be clearly seen, their inter-planar spacings are determined to be 0.254 nm and 0.127 nm, corresponding to the crystal face distances of (111) plane in MnO and (311) plane NiO, respectively. The corresponding SAED pattern is shown as the inset of Fig. 5d. Compared to the SAED pattern of the MNO hybrid (Fig. S3d, Supporting Information), the well formed rings identify the small nanocrystalline or low crystallinity of the MnO-NiO in MNG hybrid, which is certainly owing to the addition of graphene. For the electrochemical performance of electrode materials, the small nanocrystalline or low crystallinity is beneficial. In addition, it is worth noting that the MnO-NiO hybrid are stably anchored on the

graphene nanosheets even after suffering the mechanical stirring and ultrasonic treatment for a long time during the preparation of the TEM samples. That indicates the strong bonding between MnO-NiO hybrid and graphene nanosheets, which will provide considerable structure stability and simultaneously offer convenient ways for the fast electron transport from graphene matrix to MnO-NiO nanoparticles.[47] These results are consistent well with the XRD patterns. All the characteristics' analysis confirms that the MnO-NiO nanoparticles have successfully in-situ grown onto the graphene nanosheets to form a unique MNG hybrid.

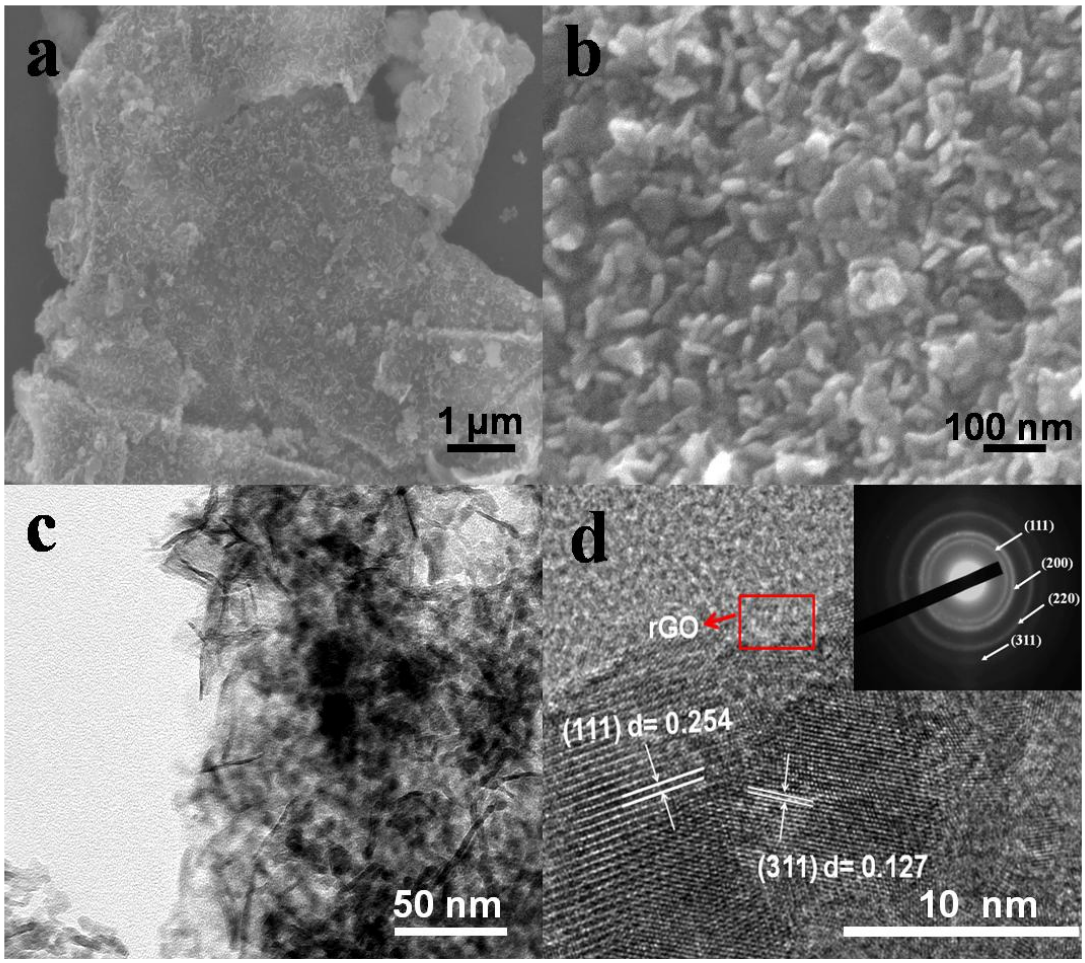

Fig. 5. MNG hybrid: (a, b) FESEM images with different magnifications; (c) TEM image; (d) HRTEM image, the inset in d is the corresponding SAED pattern.

The typical N_2 adsorption–desorption isotherms for the as-prepared MNO and MNG hybrids were investigated. The pore areas and pore volumes of the two hybrids were plotted in Fig. 6a and b for comparison. The isotherms of the samples can be recognized as type IV with an H3 hysteresis loop in the relative pressure region (0.6–1.0), indicating the mesoporous features.[48] The Brunauer–Emmett–Teller (BET) surface area of MNO and MNG were determined to be 121.11 and 179.47 $m^2 g^{-1}$, respectively. Meanwhile, the porosity of MNO and MNG were calculated via the Barrett–Joyner–Halenda (BJH) method, which displayed an average pore width of 12.21 and 12.86 nm, respectively (Fig. 6b). In addition, when MNO was processed with graphene to MNG, the pore size distribution was optimized. Part of the pore width obviously became smaller, from around 10 nm to around 2 nm and 4 nm. All the above results indicated that the introduction of graphene increased the quantity of small pores and hence the surface area of the as-prepared hybrids. Therefore, the fast diffusion of the electrolyte ions into the active hybrids can be enhanced substantially, which is beneficial for superior electrochemical performance of the as-obtained MNG hybrids as the electrode material for supercapacitors.

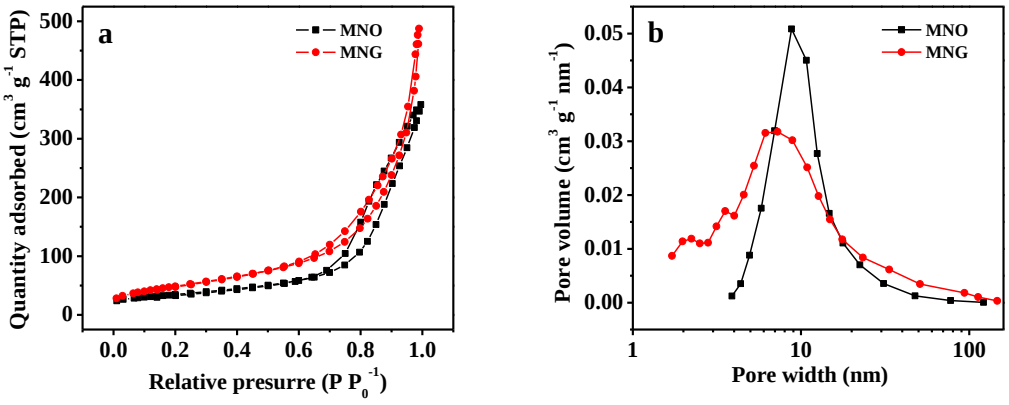

Fig. 6 (a) Typical N_2 adsorption–desorption isotherms of the as-obtained MNO and MNG hybrids and (b) the corresponding pore-size distributions.

3.3 Evaluation of electrochemical performances

The electrochemical performances of the as-prepared MNO and MNG hybrids as well as the two references of S and NS were investigated by CV and GCD measurements in 3 M KOH aqueous electrolyte (Fig. 7). No matter from the CVs or GCDs, we can obviously observe that the electrochemical performance of the MNG hybrid electrode is the best among these four as-synthesized samples, which conforms to the above physical characterizations and our initial expectation. Calculated by the discharge stages in GCDs (Fig. 7b) at 1 A g^{-1}, the specific capacitances of the electrode samples prepared by the four reaction methods (S, NS, MNO and MNG) are 176.6, 184, 407.5, 750 F g^{-1}, respectively. Namely, the capacitive performance of the MNO sample is 2.2 or 2.3 times larger than that of common coprecipitation samples with or without stirring condition, respectively, while MNG presents the best specific

capacitance which is 1.84 times of that of MNO. That is, the mixture of MnO-NiO with graphene can further improve the performance. Combining with FESEM images, the improved interface method successfully optimized the nanoscale morphology of Mn-Ni oxide and its hybrid with graphene, which caused the capacitive performance of the as-prepared electrode material to increase in multiples.

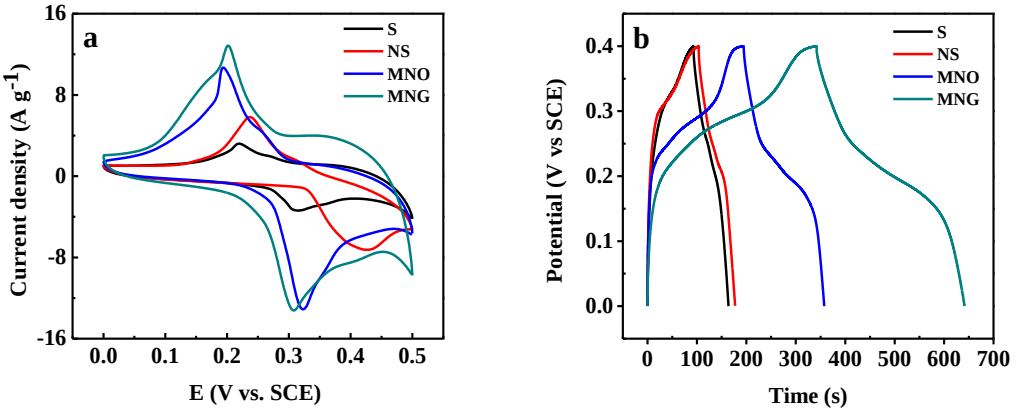

Fig. 7. (a) CV and (b) GCD curves of electrode samples prepared by different reaction modes, annealed at the same temperature 623K.

Since MNO and MNG are the two designed materials in the present work, a detail investigation of their CV and GCD curves at different scan rates (in the potential range of 0~0.5V) and at different current densities, respectively, is carried out, as shown in Fig. 8. The CV curves of MNO (Fig. 8a) and MNG (Fig. 8c) carried out at different scan rates show uniform irregular shapes with obvious redox peaks, which indicates the faradaic pseudocapacitance nature of Mn^{+2}/Mn^{+4} and Ni^{+2}/Ni^{+3} with assistance of OH^{-}.[47, 49] For both kinds of samples, the enclosed areas of CV curves

are several times larger than those of the common coprecipitation samples. That is, the improved interface method can significantly enhance the electrochemical performance of the MnO-NiO hybrid electrode material. Comparing the two improved samples, at each scanning rate, the enclosed area of MNG CVs is always larger than that of the MNO, which reflects the enhancement function of graphene. Being consistent with the CVs performance, the GCDs carried out at different current densities (Fig. 8b and d) exhibit potential changes nonlinearly with time during charging and discharging processes due to the pseudocapacitance nature.

Based on the discharge curves, The C_s is calculated drawing on the formula $C_s = I \times \Delta t/(\Delta V \times m)$, where I is the constant discharge current, t is the discharge time, and V is the potential drop during discharge sweep.[4] The calculated specific capacitances (C_s) are summarized in Fig. 8e. The values of specific capacitance of MNO and MNG hybrid electrode samples are 450 F g^{-1} and 813 F g^{-1}, respectively, at a current density of 0.5 A g^{-1}. MNG samples exhibit a high retention rate of 80.56% of specific capacitance at a high current density of 4 A g^{-1}, higher than that (69.1%) of the MNO sample (Fig. 8e). It is noteworthy mentioning that the specific capacitance of MNG hybrid outperform many other electrode materials containing Mn-Ni components or their oxides reported recently as partly shown in Table 1.

As illustrated in Fig. 8f, the electrochemical cycle performance of MNG hybrid electrode in 0~0.5 V at 4 A g^{-1} in 3M KOH aqueous electrolyte is investigated. Noticeably, after 2000 cycles, a high retention rate, about 90.1 % of the original capacitance was remained, indicating the good cycling stability of MNG hybrid electrode samples relative to the reported similar materials.[3] This high stability might be greatly attributed to the structural supporting function of the graphene nanosheets and their strong anchor effect on MnO-NiO nanoparticles. Moreover, the cycle stability of MNG is also at a relatively good level among the materials mentioned in Table 1. Although the three-electrode system test was available to study the electrochemical performance of electrode materials, apparently, the two-electrode system should be more reliable for practical application of supercapacitors. Hence, the CV and GCD measurements were also conducted in symmetric supercapacitor devices (Fig. S4a and b, Supporting Information). The energy and power densities were calculated and the corresponding Ragone plot was displayed in Fig. S4c. Furthermore, the cycle stability testing at 1 A g^{-1} was estimated in MNG//MNG symmetric supercapacitors (Fig. S4e). The specific capacitance at the initial stage was as good as 350.64 F g^{-1}, about half of the three-electrode test result. But after some subsequent cycles, certain extent attenuation occurred. Parts of the charge-discharge curves during the cycle testing were shown as Fig.S4d. The details about the

electrochemical performance of the two-electrode system were shown in supporting information (Fig. S4).

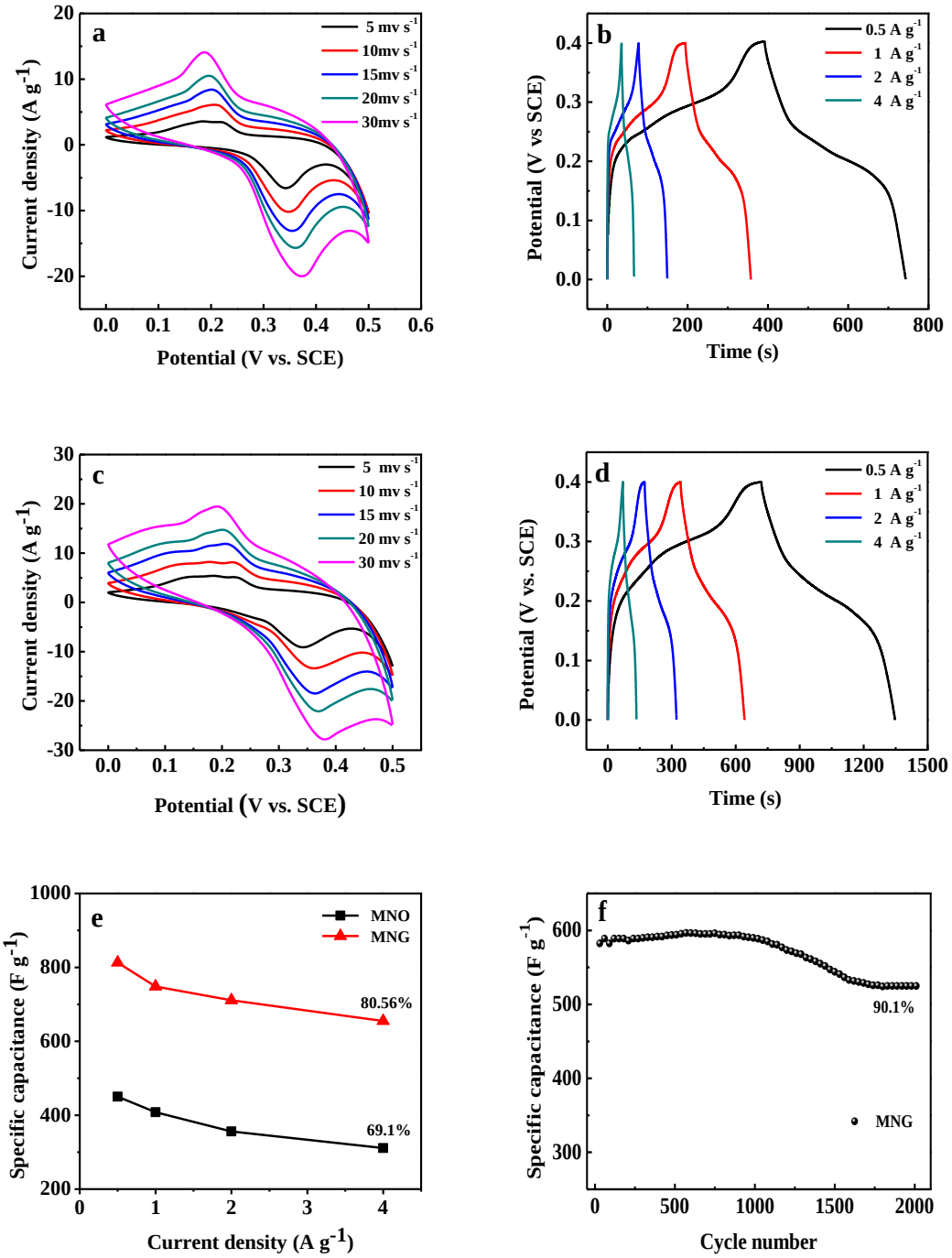

Fig. 8. (a, c) CVs at different sweep rates and (b, d) GCDs at different current densities of (a, b) MNO samples and (c, d) MNG samples, respectively; (e)the

specific capacitances of as-prepared MNO and MNG electrode samples; (f) cycle life of MNG hybrid electrode at 4 A g^{-1} in 3M KOH aqueous electrolyte.

Table 1. Comparison of capacity and cycle stability of different electrode materials containing Mn-Ni recently published.

Materials	Specific Capacitance ($F\ g^{-1}$)	Reference
Mn/Ni	210 ($5\ mV\ s^{-1}$)	50
Mn–Ni oxides	528 ($2\ mV\ s^{-1}$)	51
Mn–Ni–Cu oxides	386 ($1\ A\ g^{-1}$)	52
MnO_2 shell/Ni core	304 ($2\ A\ g^{-1}$)	53
MnO_2–CNT –graphene– Ni	251 ($1\ A\ g^{-1}$)	54

MnO@C nanocomposites	160 (1 A g^{-1})	[55]
MMCM hybrid nanowires	266 (1 A g^{-1})	[56]
MnO-NiO/rGO	750 (1 A g^{-1})	our work

The electrochemical impedance spectroscopy (EIS) for MNG and MNO hybrid electrodes was further investigated (Fig. 9). The experimental and calculated Nyquist plots of both hybrid electrodes show a nearly straight sloped line at low frequencies, which indicates the typical feature of capacitive character.[21, 33, 57] In the high frequency region, a very oblate and small semicircle are shown on both plots, corresponding to a parallel combination of charge transfer resistance (R_{ct}) and double-layer capacitance, declaring simple kinetics for charge transfer into the reaction zone of the improved interface system. The intercepts of both plots with the real axis (Z') give small equivalent series resistance (ESR) values which are essentially favorable for high capacitance of supercapacitors. To further investigate the impedance behaviors, EIS data was fitted with an equivalent circuit derived from the Nyquist plots. In the equivalent circuit, R_s is the bulk solution resistance, R_{ct} is the charge

transfer resistance, Q is the constant phase element which accounts for a double-layer capacitance, W is the Warburg impedance, and C is the Faradaic pseudocapacitor. In detail, R_s and R_{ct} of the MNO and MNG hybrid electrodes were calculated to be 0.64 Ω, 0.4021 Ω and 0.4238 Ω, 0.2525 Ω, respectively. Obviously, the resistance of both MNG and MNO hybrid electrodes is quite low, indicating the excellent conductivity of the as-prepared active material. In addition, the decrease of the R_s and R_{ct} values from MNO to MNG directly highlights the advantageous effect of composite graphene on enhancing the conductivity of the as-obtained hybrids. Therefore, the analysis result of the EIS confirms again that MNO and MNG hybrids are both ideal high capacitive materials and MNG is the better one.

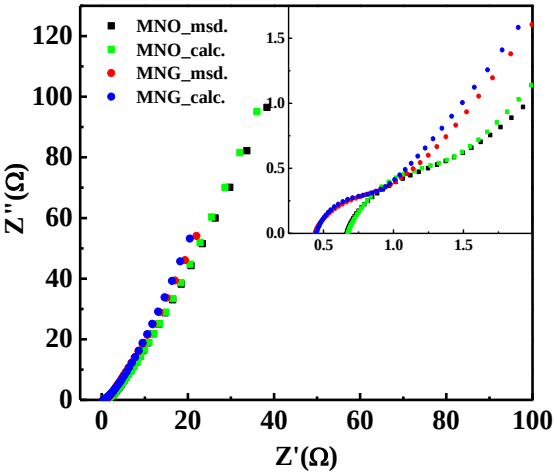

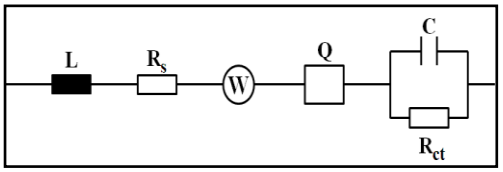

materials	R_s(Ω)	R_{ct}(Ω)
MNO	0.64	0.4021
MNG	0.4238	0.2525

Fig. 9. The experimental (msd.) and calculated (calc.) Nyquist plots for MNO and MNG electrode samples and the inset displays the enlarged high frequency portions of the plots; The right part shows the equivalent circuit derived from the Nyquist plots and the corresponding calculated resistance values.

4. Conclusions

In summary, a novel and facile one-step improved interface synthesis route has been exploited to in-situ grow MnO-NiO nanoparticles onto the graphene nanosheets for supercapacitor electrode materials. Especially, the improved reaction system played a key role. The agglomeration problem of common coprecipitation method was successfully solved without using any complex process. The uniformly distributed MnO-NiO nanoparticles with large specific area, supported by graphene nanosheets with excellent conductivity, guarantee a high specific capacitance (813 F g^{-1} at 0.5 A g^{-1}) and excellent rate capability (80.56% retention at 4A g^{-1}) and good cycling stability. Furthermore, the present improved interface method has the possibility to be applied for many other kinds of inorganic salts like zinc, iron, copper and aluminum, so it may be extended to a wider variety of electrode materials for supercapacitors and more widespread technology applications.

Acknowledgment

This work was financially supported by the Foundation of National Key Basic Research and Development Program (No.2010CB631001).

References

1. V. Subramanian, H. Zhu, R. Vajtai, P. Ajayan and B. Wei, *The Journal of Physical Chemistry B*, 2005, **109**, 20207-20214.

2. A. Leela Mohana Reddy, F. Estaline Amitha, I. Jafri and S. Ramaprabhu, *Nanoscale Research Letters*, 2008, **3**, 145-151.

3. S. Chen, J. Zhu, X. Wu, Q. Han and X. Wang, *ACS nano*, 2010, **4**, 2822-2830.

4. S.-J. Bao, C. M. Li, C.-X. Guo and Y. Qiao, *Journal of Power Sources*, 2008, **180**, 676-681.

5. F. Cao, G. X. Pan, X. H. Xia, P. S. Tang and H. F. Chen, *Journal of Power Sources*, 2014, **264**, 161-167.

6. C. Liu, F. Li, L. P. Ma and H. M. Cheng, *Advanced materials*, 2010, **22**, E28-62.

7. B. Babakhani and D. G. Ivey, *Journal of Power Sources*, 2010, **195**, 2110-2117.

8. Y.-T. Wang, A.-H. Lu and W.-C. Li, *Microporous and Mesoporous Materials*, 2012, **153**, 247-253.

9. W. Wei, X. Cui, W. Chen and D. G. Ivey, *Chemical Society Reviews*, 2011, **40**, 1697-1721.

10. Q. Wang, Z. Wen and J. Li, *Advanced Functional Materials*, 2006, **16**, 2141-2146.

11. S. I. Kim, J. S. Lee, H. J. Ahn, H. K. Song and J. H. Jang, *ACS applied materials & interfaces*, 2013, **5**, 1596-1603.

12. X.-h. Xia, J.-p. Tu, Y.-j. Mai, X.-l. Wang, C.-d. Gu and X.-b. Zhao, *Journal of Materials Chemistry*, 2011, **21**, 9319.

13. Q. Zhang, E. Uchaker, S. L. Candelaria and G. Cao, *Chemical Society Reviews*, 2013, **42**, 3127-3171.

14. S. L. Brock, N. Duan, Z. R. Tian, O. Giraldo, H. Zhou and S. L. Suib, *Chemistry of Materials*, 1998, **10**, 2619-2628.

15. T. N. Ramesh and P. V. Kamath, *Journal of Power Sources*, 2008, **175**, 625-629.

16. M. Zhang, S. Guo, L. Zheng, G. Zhang, Z. Hao, L. Kang and Z.-H. Liu, *Electrochimica Acta*, 2013, **87**, 546-553.

17. M.-S. Wu, C.-H. Yang and M.-J. Wang, *Electrochimica Acta*, 2008, **54**, 155-161.

18. D. Zhai, B. Li, H. Du, G. Gao, L. Gan, Y. He, Q. Yang and F. Kang, *Carbon*, 2012, **50**, 5034-5043.

19. D. Su, *Chemical Communications*, 2012, **48**, 7149-7151.

20. A. Pendashteh, M. F. Mousavi and M. S. Rahmanifar, *Electrochimica Acta*, 2013, **88**, 347-357.

21. W. Xiao, D. Hu, C. Peng and G. Z. Chen, *ACS applied materials & interfaces*, 2011, **3**, 3120-3129.

22. R. Jiang, T. Huang, J. Liu, J. Zhuang and A. Yu, *Electrochimica Acta*, 2009, **54**, 3047-3052.

23. C. Yuan, L. Hou, L. Yang, D. Li, L. Shen, F. Zhang and X. Zhang, *Journal of Materials Chemistry*, 2011, **21**, 16035.

24. W. S. Hummers Jr and R. E. Offeman, *Journal of the American Chemical Society*, 1958, **80**, 1339-1339.

25. N. I. Kovtyukhova, P. J. Ollivier, B. R. Martin, T. E. Mallouk, S. A. Chizhik, E. V. Buzaneva and A. D. Gorchinskiy, *Chemistry of Materials*, 1999, **11**, 771-778.

26. L. Feng, Y. Zhu, H. Ding and C. Ni, *Journal of Power Sources*, 2014, **267**, 430-444.

27. X.-h. Xia, J.-p. Tu, X.-l. Wang, C.-d. Gu and X.-b. Zhao, *J. Mater. Chem.*, 2011, **21**, 671-679.

28. B. Koo, H. Xiong, M. D. Slater, V. B. Prakapenka, M. Balasubramanian, P. Podsiadlo, C. S. Johnson, T. Rajh and E. V. Shevchenko, *Nano letters*, 2012, **12**, 2429-2435.

29. Z. Fan, K. Wang, T. Wei, J. Yan, L. Song and B. Shao, *Carbon*, 2010, **48**, 1686-1689.

30. Y. Ye, L. Kuai and B. Geng, *Journal of Materials Chemistry*, 2012, **22**, 19132.

31. Q. Lu, J. G. Chen and J. Q. Xiao, *Angewandte Chemie*, 2013, **52**, 1882-1889.

32. Y.-T. Wang, A.-H. Lu, H.-L. Zhang and W.-C. Li, *The Journal of Physical Chemistry C*, 2011, **115**, 5413-5421.

33. Q. Lu and Y. Zhou, *Journal of Power Sources*, 2011, **196**, 4088-4094.

34. W. Chen, L. Yan and P. R. Bangal, *Carbon*, 2010, **48**, 1146-1152.

35. J. Li, W. Zhao, F. Huang, A. Manivannan and N. Wu, *Nanoscale*, 2011, **3**, 5103.

36. H. Y. Chu, Q. Y. Lai, Y. J. Hao, Y. Zhao and X. Y. Xu, *Journal of Applied Electrochemistry*, 2009, **39**, 2007-2013.

37. S. Park, K.-S. Lee, G. Bozoklu, W. Cai, S. T. Nguyen and R. S. Ruoff, *ACS nano*, 2008, **2**, 572-578.

38. K. Subramani, D. Jeyakumar and M. Sathish, *Physical chemistry chemical physics : PCCP*, 2014, **16**, 4952-4961.

39. L. Zhang, L. Zhao and J. Lian, *RSC Advances*, 2014, **4**, 41838-41847.

40. Z. Liu, R. Ma, M. Osada, N. Iyi, Y. Ebina, K. Takada and T. Sasaki, *Journal of the American Chemical Society*, 2006, **128**, 4872-4880.

41. J. Fang, M. Li, Q. Li, W. Zhang, Q. Shou, F. Liu, X. Zhang and J. Cheng, *Electrochimica Acta*, 2012, **85**, 248-255.

42. S. G. Kandalkar, J. L. Gunjakar and C. D. Lokhande, *Applied Surface Science*, 2008, **254**, 5540-5544.

43. S.-G. Hwang, S.-H. Ryu, S.-R. Yun, J. M. Ko, K. M. Kim and K.-S. Ryu, *Materials Chemistry and Physics*, 2011, **130**, 507-512.

44. G. He, L. Wang, H. Chen, X. Sun and X. Wang, *Materials Letters*, 2013, **98**, 164-167.

45. Y.-Z. Su, K. Xiao, N. Li, Z.-Q. Liu and S.-Z. Qiao, *Journal of Materials Chemistry A*, 2014, **2**, 13845-13853.

46. T. Kuila, A. K. Mishra, P. Khanra, N. H. Kim and J. H. Lee, *Nanoscale*, 2013, **5**, 52-71.

47. J. Zhao, J. Chen, S. Xu, M. Shao, Q. Zhang, F. Wei, J. Ma, M. Wei, D. G. Evans and X. Duan, *Advanced Functional Materials*, 2014, **24**, 2938-2946.

48. M. Kruk and M. Jaroniec, *Chemistry of Materials*, 2001, **13**, 3169-3183.

49. Z. Tang, C.-h. Tang and H. Gong, *Advanced Functional Materials*, 2012, **22**, 1272-1278.

50. H. Kim and B. N. Popov, *Journal of The Electrochemical Society*, 2003, **150**, D56.

51. D.-L. Fang, B.-C. Wu, Y. Yan, A.-Q. Mao and C.-H. Zheng, *Journal of Solid State Electrochemistry*, 2011, **16**, 135-142.

52. D.-L. Fang, Z.-D. Chen, B.-C. Wu, Y. Yan and C.-H. Zheng, *Materials Chemistry and Physics*, 2011, **128**, 311-316.

53. D. Liu, Q. Wang, L. Qiao, F. Li, D. Wang, Z. Yang and D. He, *J. Mater. Chem.*, 2012, **22**, 483-487.

54. G. Zhu, Z. He, J. Chen, J. Zhao, X. Feng, Y. Ma, Q. Fan, L. Wang and W. Huang, *Nanoscale*, 2014, **6**, 1079-1085.

55. T. Wang, Z. Peng, Y. Wang, J. Tang and G. Zheng, *Scientific reports*, 2013, **3**, 2693.

56. H. Jiang, L. Yang, C. Li, C. Yan, P. S. Lee and J. Ma, *Energy & Environmental Science*, 2011, **4**, 1813.

57. S. W. Zhang and G. Z. Chen, *Energy Materials*, 2008, **3**, 186-200.